A Hub-type Compliant Piezo Drill for Cell Microinjection*

Yuzhou Duan, Yunzhi Zhang, Jie Ling, *Member, IEEE,* Zhao Feng, and Yuchuan Zhu, *Member, IEEE*

***Abstract*— Robotic-assisted cell microinjection is widely used in biological areas. However, the large lateral vibrations of the pipette tip do great harm to cell membranes. In this paper, a spatial hub-type compliant mechanism (CM) applied in high-frequency penetration is proposed to reduce the vibration. By using the building blocks approach, the structure synthesis is done to design the hub-type CM. A static model is established by using the flexibility matrix method, and a dynamic model is established by using the lumped parameters method. Based on proposed design goals, parameter optimization of the CM is performed. The finite element simulations are conducted to verify the established analytical models. The results show that the RMS error of the static model and dynamic model is 0.73% and 6.1% respectively. To test the vibration rejection performance of the designed CM in a microinjection environment, an injection device equipped with the proposed hub-type CM is built and simulations are performed in comparison with a traditional injection device in the COMSOL software environment. Results show that the designed hub-type CM can well reduce the lateral vibration (i.e., 5.75 times in peak value).**

I. INTRODUCTION

Cell microinjection is long-lasting and full of vitality technology in drug development, artificial insemination, cancer study and other biological research [1-4]. It utilizes injection pipettes to implement penetration and injection, in turn, to deliver exogenous substances into cells. During the whole process, penetration is a significant step, which was implemented by manual incipiently [5]. With the growth of automation technology, efficient robotic-assisted penetration is developed to replace artificial operations [6]. In addition, piezo-stack actuators (PSAs) are widely adopted due to the characteristics of fast response and high resolution [7].

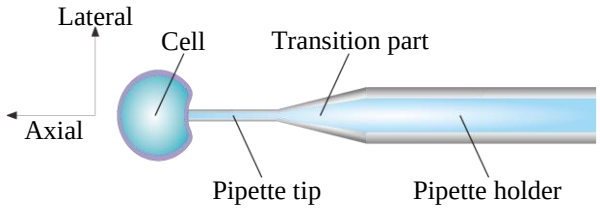

Fig. 1: Schematic of pipettes puncture into cells

At present, one of the main problems for robotic-assisted penetration is the sustained large cell deformation in the penetration step. As shown in Fig. 1, the undesired deformation will lead to cell damage and further decrease the survival rate of the samples [8]. Two reasons mainly cause the unwanted deformation. One is that the membrane is thick and high elastic [9], resulting in precious control of puncture force and velocity. The other is that the PSAs in robotic-assisted penetration cause large undesired lateral vibrations of the tip of the injection pipette [10], which also leads to large cell deformation.

Penetration strategies have been developed to reduce cell damage. Low-frequency penetration strategies are adopted in early robotic-assisted penetration. An example is the pulse-based penetration strategy [11], where several piezo pulses are applied to break the zona pellucida and membranes of mouse oocytes. However, the usage of mercury to suppress lateral vibration is toxic to cells. A rotational drilling strategy was developed in [12], utilizing the pipette's rotational motion to implement penetration. Although this strategy is mercury-free, it has high requirements for the symmetry of the rotational part. Microdynamics of the pipettes were studied in [13]. The results declared that lateral dynamics play an important role in piercing cell membranes in low-frequency penetration (i.e., 2 Hz).

An unavoidable issue for low-frequency penetration strategies is the control of the puncture force and velocity of the pipette tip. Strategies in high-frequency vibration penetration (HFVP) were put on the map for solving this problem. In [14], lateral vibration energy is mainly used to break the membrane. But the lateral vibration amplitude (17 μm) is still too large as far as small-diameter cells (e.g. 200 μm) are concerned. Therefore, the large lateral vibration remains a crucial problem in HFVP. Recently, it was found that cells can also be punctured harmlessly even with lateral vibration significantly reduced (e.g. 2 μm) in high-frequency conditions [15]. Based on this, a flexure-guided compliance mechanism (CM) aiming at reducing the lateral vibration was designed. However, the proposed CM could not eliminate the parasitic movement out of the plane.

In brief summary, HFVP is considered to be a more harmless way both for cells and the operators. To decrease the lateral vibration in HFVP, CMs are introduced to perform the guidance effect. To the authors best knowledge, the study of spatial configured CMs remains empty in HFVP. In comparison with current planar CMs, spatial configured CMs can eliminate the parasitic movement out of the plane and further decrease the lateral vibration.

With the HFVP beginning to reflect its advantages, the lateral vibration of the pipette tip needs to be ulteriorly reduced. This paper mainly contributes to proposing a spatial

*This work was supported by the Natural Science Foundation of Jiangsu Province (Grant No. BK20210294); the National Undergraduate Innovation and Entrepreneurship Program (Grant No. 202110287128Y).

Yuzhou Duan, Yunzhi Zhang, Jie Ling, and Yuchuan Zhu are with the College of Mechanical and Electrical Engineering, Nanjing University of Aeronautics and Astronautics, 210016 Nanjing, China.

Zhao Feng is with Faculty of Science and Technology, University of Macau, Macao SAR 999078, China.

Corresponding author: Jie Ling meejling@nuaa.edu.cn

hub-type CM that has well performance in HFVP. In this paper, design goals are proposed as the outline of the design first. Next, the building blocks approach (BBA) is used for structure synthesis. A static model and a dynamic model are established by using the flexibility matrix method (FMM) and the lumped parameters method (LPM), respectively. Then parameter optimization is done and the finite element method (FEM) model of the CM is established. Simulations are done to validate the correctness of the two analytical models. An injection device equipped with the proposed hub-type CM is built and simulations are performed in comparison with a traditional injection device in the COMSOL software environment to test the vibration rejection performance of the designed CM.

The rest of this paper is organized as follows. Section II presents the design goals of CMs. Section III proposes the configuration of the spatial hub-type structure CM by structure synthesis. A static model and a dynamic model of the designed CM are developed in Section IV and Section V, respectively. In Section VI, the geometric parameters of the CM are optimized. In Section VI. The FEM models are established to validate the analytical models. Performance test of the injection device with hub-type CM is done through a comparison study. Conclusions of the results and future work are given in Section VII.

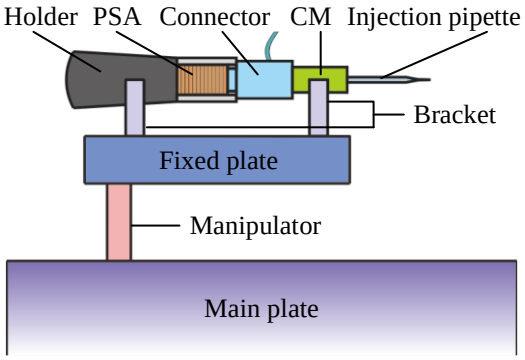

Fig. 2: Schematic of the traditional injection device with compliant mechanisms.

II. STRUCTURE DESIGN

In this section, design goals are proposed for HFVP by analyzing the working environment of the injection device. Then structure synthesis is used to obtain the configuration of the so-called hub-type CM.

A. Design Goals

One traditional injection device with CM is shown in Fig. 2. The injection pipette is fixed on one clipped CM and is driven by an axially-moving PSA. By analyzing the environment and mechanism of the device, the following design goals are proposed to design a CM for HFVP.

- Fatigue fracture due to stress concentration needs to be considered in CM, especially in high-frequency conditions.

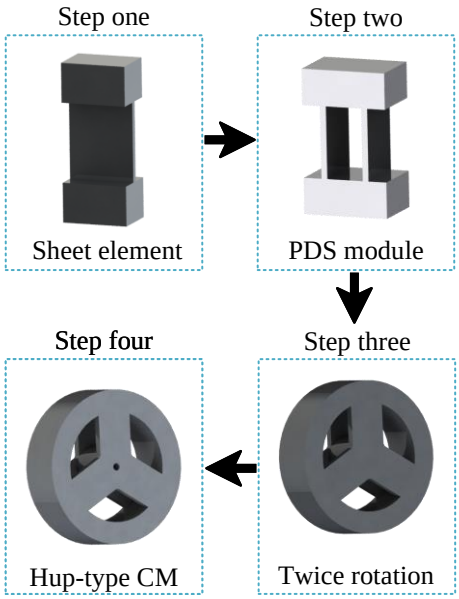

Fig. 3: Structure design of the hub-type CM by using the building blocks approach.

- Degrees of freedom (DOFs) except for the axial rotation and the axial motion should be restricted to avoid lateral displacement.
- The axial first-order natural frequency of the CM should be designed a little higher than the working frequency to ensure sufficient axial output without damaging the CM.

B. Structure Synthesis

BBA can obtain the wanted configuration of the CM efficiently. In this paper, this approach is used to design the structure of the CM. As shown in Fig. 3, according to the first proposed design goal, sheet units are chosen as the deformation sources to reduce the stress concentration. Next, a one DOF planar parallel-double-sheets (PDS) module is assembled from the units. To eliminate the lateral parasite movement and reduce disturbance out of the plane, a spatial circumferential symmetry structure is obtained by rotating the PDS module twice. In addition, a hole for fixing the injection pipette is designed. The final configuration is the so-called hub-type CM.

III. STATIC MODELING

To meet the second design goal, relative DOFs between the functional direction and the restricted direction should be depicted. The stiffness ratio between each direction is one effective way to represent the relative DOFs. Having the hub-type configuration of the designed CM, the analytical static model is established in this section to obtain the stiffness ratio.

A. Setting of Coordinate Systems

As shown in Fig. 4(a), the coordinate system $oxyz$ is the reference coordinate system, and the coordinate systems

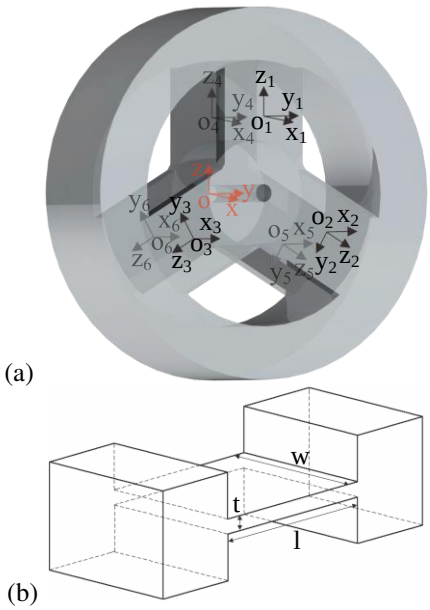

Fig. 4: Setting of the hub-type CM. (a) The reference coordinate system and the local coordinate systems of the hub-type CM. (b) The geometric parameters of the sheet element.

$o_i x_i y_i z_i$ are the local coordinate systems (the subscript i refers to the number of each sheet unit). For each local coordinate system $o_i x_i y_i z_i$, the z_i axis points out of the structure along the length direction of the sheet unit. The x_i axis points along the output direction of the CM. The y_i axis is perpendicular to the other two axes and its positive direction conforms to the right-hand rule. The orientation of $oxyz$ is same as $x_1 y_1 z_1$. The origin of each local coordinate system is located in the geometric center of each sheet element. The origin of the reference coordinate system is located in the geometric center of the plane of the CM's bottom.

B. Global Flexibility Matrix

The relationship between the generalized force T and the generalized displacement W is

$$T = \mathbf{C}W \tag{1}$$

where

$$T = [\theta_x \quad \theta_y \quad \theta_z \quad \delta_x \quad \delta_y \quad \delta_z]'$$

$$W = [M_x \quad M_y \quad M_z \quad F_x \quad F_y \quad F_z]'$$

where x, y, z is the directional subscript, θ is the rotation angle, δ is the displacement, F is the applied force, and M is the applied moment. The matrix $\mathbf{C}$ is the flexibility matrix.

Based on the previous local coordinate systems in Fig. 4(a) and the geometric parameters in Fig. 4(b). The local flexibility matrix C_l of each sheet unit can be represented as

$$C_l = \frac{l}{EI_y}\begin{bmatrix} \alpha & & & & & \\ & 1 & & & & \\ & & \frac{1}{4\chi} & & & \\ & & & \frac{l^2}{12} & & \\ & & & & \frac{l^2}{12}\alpha & \\ & & & & & \frac{l^2}{12}\beta \end{bmatrix} \tag{2}$$

where $\alpha = (\frac{t}{w})^2, \beta = (\frac{t}{l})^2, \chi = \frac{G}{E}$. E is the elastic modulus, G is the shear modulus, and I_y is the area moment of inertia to the y-axis.

The coordinate transformation matrix Ad_i is introduced to transform the local flexibility matrix into one collective coordinate system

$$Ad_i = \begin{bmatrix} R_i & 0 \\ \hat{t}R_i & R_i \end{bmatrix} \tag{3}$$

where R_i is the rotation matrix between the local coordinate systems and the global coordinate system. i is the subscript of each sheet unit. $\hat{t}$ is the anti-symmetric matrix, which takes the form

$$\hat{t} = \begin{bmatrix} 0 & -z & y \\ z & 0 & -x \\ -y & x & -0 \end{bmatrix} \tag{4}$$

Since the six units are parallel connected, the global flexibility matrix C_g of the CM can be assembled by the following equation

$$C_g = (\sum_{i=1}^{n}(Ad_i C_l Ad_i)^{-1})^{-1} \tag{5}$$

Marking c_{gd} is a vector that contains the diagonal elements of the global flexibility matrix, one has

$$c_{gd} = diag(C_g) = [c_{g11}, c_{g22}, c_{g33}, c_{g44}, c_{g55}, c_{g66}] \tag{6}$$

Substitution of (2) (3) and (4) into (5) gives

$$\begin{cases} c_{g11} = \frac{l}{EI_y}\frac{\alpha}{24}, \\ c_{g22} = \frac{l}{EI_y}\frac{\alpha\beta l^2}{3(3L^2\alpha+3L^2\beta+4\alpha\beta l^2+4\alpha\beta l^2\chi))}, \\ c_{g33} = \frac{l}{EI_y}\frac{\alpha\beta l^2}{3(3L^2\alpha+3L^2\beta+4\alpha\beta l^2+4\alpha\beta l^2\chi))}, \\ c_{g44} = \frac{l}{EI_y}\frac{l^2}{72}, \\ c_{g55} = \frac{l}{EI_y}\frac{\alpha\beta l^2(3L^2\alpha+3L^2\beta+2\alpha\beta l^2+2\alpha\beta l^2\chi)}{18(\alpha+\beta)(3L^2\alpha+3L^2\beta+4\alpha\beta l^2+4\alpha\beta l^2\chi)}, \\ c_{g66} = \frac{l}{EI_y}\frac{\alpha\beta l^2(3L^2\alpha+3L^2\beta+2\alpha\beta l^2+2\alpha\beta l^2\chi)}{18(\alpha+\beta)(3L^2\alpha+3L^2\beta+4\alpha\beta l^2+4\alpha\beta l^2\chi)}, \end{cases} \tag{7}$$

Eq. (7) is the analytical expression of the diagonal elements of the global flexibility matrix.

C. Analytical Stiffness Ratio

According to the definition, c_{g11} has no effect on the lateral vibration, c_{g22} represents the flexibility in functional direction, and the other four elements represent the flexibility causing lateral displacement. In addition, notice that the six elements have the following relationship

$$c_{g22} = c_{g33}, c_{g55} = c_{g66} \tag{8}$$

So only two stiffness ratios need to be considered. Nondimensionalizing the parameters, the two stiffness ratios take the form

$$k_1 = \frac{c_{g44}}{c_{g22}l^2} = \frac{3\eta^2\alpha + 3\eta^2\beta + 4\alpha\beta + 4\alpha\beta\chi}{24\alpha\beta} \tag{9a}$$

$$k_2 = \frac{c_{g44}}{c_{g55}} = \frac{(\alpha+\beta)(3\eta^2\alpha + 3\eta^2\beta + 4\alpha\beta + 4\alpha\beta\chi)}{4\alpha\beta(3\eta^2\alpha + 3\eta^2\beta + 2\alpha\beta + 2\alpha\beta\chi)} \tag{9b}$$

where $\eta = \frac{L}{l}$. k_1 and k_2 are the two needed analytical stiffness ratios representing the relative DOFs.

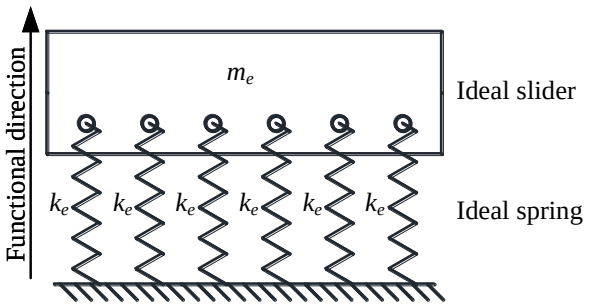

Fig. 5: The schematics of the simplified dynamic model by using lumped parameters method.

IV. DYNAMIC MODELING

In this section, a simplified parallel spring-slider model is proposed by using the LPM. The analytical first-order natural frequency of the CM is obtained to meet the third proposed design goal.

A. Simplified Parallel Spring-slider Model

By using the LPM, the proposed CM can be simplified into a parallel spring-slider model, as shown in Fig. 5. k_e and m_e are the functional direction equivalent stiffness and the equivalent mass respectively.

According to (2), the equivalent stiffness k_e takes the form

$$k_e = \frac{1}{c_{l44}} = \frac{12EI_y}{l^3} \tag{10}$$

The equivalent mass m_e consists of two parts

$$m_e = \overline{m_s} + \overline{m_c} \tag{11}$$

where $\overline{m_s}$ and $\overline{m_c}$ are from the sheet unit and the inner cylinder respectively.

Because the displacement of the centroid of the sheet unit is about 1/2 of the displacement of the center cylinder, $\overline{m_s}$ and $\overline{m_c}$ take the form

$$\begin{cases} \overline{m_s} = \frac{3\rho tlw}{2}, \\ \overline{m_c} = \rho\pi L(R^2 - r^2) \end{cases} \tag{12}$$

where ρ is the material density of the CM, L is the length of the cylinder, R is the outer radius of the cylinder, r is the radius of the inner hole of the cylinder.

The first-order natural frequency of the simplified model takes the form

$$f = \frac{1}{2\pi}\sqrt{\frac{6k_e}{m_e}} \tag{13}$$

Substitution of (10) (11) (12) into (13) gives

$$\overline{f} = \frac{1}{2\pi}\sqrt{\frac{3Et^3w}{l^3\left(3\,l\,\rho\,t\,w + 2\pi\,L\,\rho\,(R^2 - r^2)\right)}} \tag{14}$$

Eq. (14) is the analytical solution of the first-order natural frequency.

V. TWO DESIGN PARAMETERS

In the previous article, based on the design goals, parameters of the stiffness ratio and the first-order natural frequency are obtained. In this section, two design parameters are proposed for the design of the hub-type CM through reasonable assumptions and simplification.

A. Design Parameter: Relative DOFs

Notice that the geometric parameters of the sheet units comply with the following rules

$$\alpha \ll 1, \beta \ll 1, \alpha\beta \ll \alpha, \alpha\beta \ll \beta \tag{15}$$

So (9a) and (9b) can be simplified to

$$\begin{cases} k_1' = \frac{\eta^2}{8}\frac{\alpha+\beta}{\alpha\beta}, \\ k_2' = \frac{\alpha+\beta}{4\alpha\beta} \end{cases} \tag{16}$$

Due to the minimum value of k_1' and k_2' determines the minimum stiffness of the hub-type CM, they can be simplified in one parameter by equalizing them. The result takes the form

$$\eta = \frac{L}{l} = \sqrt{2} \tag{17}$$

One uniform characteristic parameter $\overline{k}$ can be obtained to represent the two stiffness ratios

$$\overline{k} = \frac{\alpha+\beta}{4\alpha\beta} \tag{18}$$

Substitution of parameters gives

$$\overline{k} = \frac{l^2 + w^2}{4t^2} \tag{19}$$

where $\overline{k}$ is the design parameter representing the relative DOFs.

B. Design Parameter: First-order Natural Frequency

Substitution (17) into (14) and expanded expression gives

$$\overline{f} = \frac{1}{2\pi}\sqrt{\frac{3Et^3w}{l^3\left(3\,l\,\rho\,t\,w + 2\sqrt{2}\,\pi\,l\,\rho\,(R^2 - r^2)\right)}} \tag{20}$$

where $\overline{f}$ is the design parameter representing the first-order natural frequency.

VI. PARAMETER OPTIMIZATION

According to the above analysis, structural optimization is carried out. The optimization objective is to maximize the first-order natural frequency $\overline{f}$. The optimization objects are the geometric parameters of the sheet unit l, t, and w.

Constraints are listed as follows:

$$\begin{cases} \overline{k} \geq 10 \\ t/w \leq 0.2 \\ t/l \leq 0.2 \\ t \geq 0.5 \\ w \leq \sqrt{3}R \\ l/R \geq 5 \end{cases} \tag{21}$$

The material of the injection pipette is borosilicate (CORNING 7740). The material of hub-type CMs is structural steel. Properties of these two materials are shown in TABLE I. η is the isotropic loss factor, and μ is the Poisson ratio. Matlab Optimization Toolbox was used to set the initial value of the parameters $[t, l, w] = [1, 20, 5.2]$. The constants R and r and optimization results are shown in TABLE II.

TABLE I: Material properties of the injection device

	$E(Pa)$	$\rho(kg/m^3)$	μ	η
CORNING 7740	$62.75e^9$	2230	0.2	$15e^{-5}$
Structure steel	$160e^9$	7850	0.29	0.01

TABLE II: Geometric parameters of the hub-type CM

Geometric parameters	R	r	t	l	w
Value	3.5	0.5	1.2	17.5	6.1

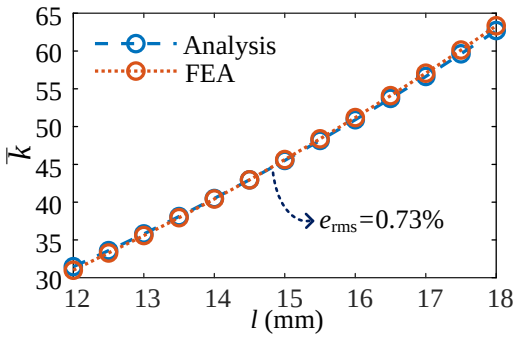

Fig. 6: Analytical and FEA results of the design parameter $\overline{k}$ with the different length of the sheet unit l.

VII. VALIDATION AND TEST

FEM model of the hub-type CM is established based on the optimized parameters in the COMSOL software environment. The proposed analytical models are validated first. Then an injection device with hub-type CM is proposed in comparison with a traditional CM to test the characteristics of the CM.

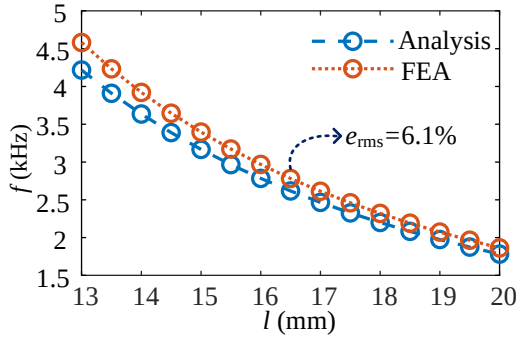

Fig. 7: Analytical and FEA results of the first-order frequency with the different length of the sheet unit l.

A. Validation of the Analytical Models

1) Static Model Validation: To verify the static model, finite element analysis of the design parameter $\overline{k}$ was performed with different l. The analytical and numerical results are in consistent agreement, as shown in Fig. 6. The root-mean-square error between the two models is 0.73%.

2) Dynamic Model Validation: The first-order natural frequency solution of the analytical model and FEM model are also calculated to verify the accuracy of the proposed analytical model. The results are shown in Fig. 7. By comparing the first-order natural frequency with different l, we found the root-mean-square error between the two models is 6.1%. The error may be caused by the equivalent mass error of the LPM.

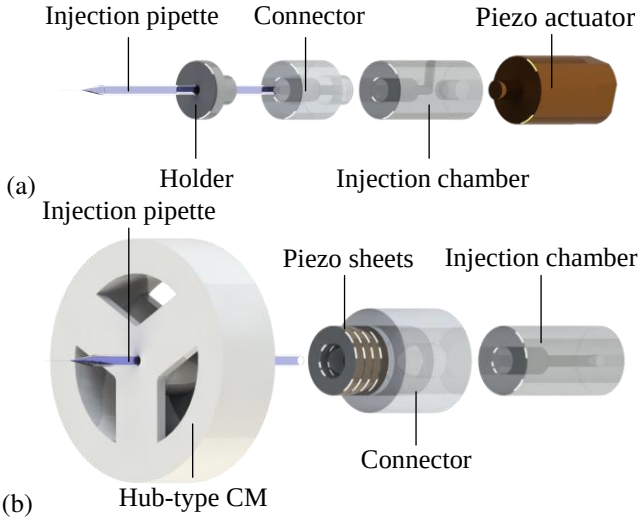

Fig. 8: Schematics of two kinds of injection devices for comparison (a) A traditional type microinjection device in [14]. (b) This injection device with hub-type compliant mechanisms.

B. Hub-type CMs Characteristic Test

A traditional piezo-assisted injection device is shown in Fig. 8(a). In order to test the proposed hub-type CM, a new type of injection device equipped with the hub-type CM is

proposed in Fig. 8(b) in comparison with the traditional one. Remarkably, the hub-type CM provides the pre-pressure to the piezoelectric sheets (instead of using the encapsulated PSAs). In this way, the structure of the microinjection device can be more compact, which reduces the assembly error.

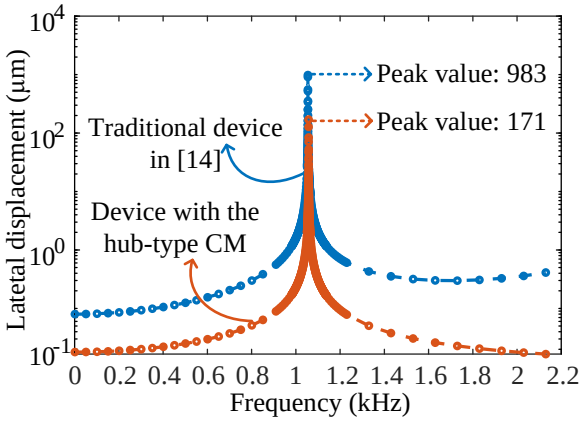

Fig. 9: Comparison study: the lateral vibration amplitude of the pipette tip under sinusoidal frequency sweep.

The frequency sweep test is given to test the performance of the hub-type CM in comparison with the traditional one [14]. The lateral vibration of the pipette tip is generated by the lateral excitation source, transmitted and amplified by the cantilever beam structure (the pipette holder), then finally causes great damage to the cells in the pipette tip. In this test, a lateral sinusoidal excitation source (80 nm, from the previous article [13]) is applied at the bottom of the injection pipette. The frequency of the excitation source is swept from 1 Hz to 2.2 kHz (the first-order natural frequency of the hub-type CM). The stationary lateral vibration amplitude of the pipette tip is calculated. The result in Fig. 9 shows that in comparison with the traditional one, the proposed device can better reduce the lateral vibration (5.75 times in peak value).

VIII. Conclusion

This paper reports the design, modeling, and test of a hub-type CM with the purpose of reducing lateral vibration in high-frequency vibration penetration. By establishing the analytical models, two design parameters are obtained for parameter optimization. The accuracy of the analytical model is validated through FEM simulation. Comparative studies are performed to validate the characteristics of the hub-type CM. Results show that the proposed structure is effective to suppress the lateral vibration.

During the study, insufficiency is also found and listed as follows for future improvements.

- Because the structure of the hub-type CM is hard to fabricate by machining, 3D print technology is planned to fabricate this CM. Due to the low accuracy of metal printing, new material for substitution needs to be applied to obtain the prototype of the CM.
- In this paper, only the sinusoidal disturbance is considered. In practice, the disturbance is multisource and multiform. So more complicated conditions need to be introduced and tested in future study.

References

[1] S. Babu Reddiar, H. Al-Wassiti, C. W. Pouton, C. J. Nowell, M. A. Matthews, A. Rahman, N. Barlow, and R. S. Norton, "Assessing the cellular toxicity of peptide inhibitors of intracellular protein-protein interactions by microinjection," *Bioorganic & Medicinal Chemistry*, vol. 29, p. 115906, 2021.

[2] Y. Wei and Q. Xu, "A survey of force-assisted robotic cell microinjection technologies," *IEEE Transactions on Automation Science and Engineering*, vol. 16, no. 2, pp. 931–945, 2019.

[3] F. Pan, S. Chen, Y. Jiao, Z. Guan, A. Shakoor, and D. Sun, "Automated high-productivity microinjection system for adherent cells," *IEEE Robotics and Automation Letters*, vol. 5, no. 2, pp. 1167–1174, 2020.

[4] P. Letrado, H. Mole, M. Montoya, I. Palacios, J. Barriuso, A. Hurlstone, R. Dez-Martnez, and J. Oyarzabal, "Systematic roadmap for cancer drug screening using zebrafish embryo xenograft cancer models: melanoma cell line as a case study," *Cancers*, vol. 13, no. 15, 2021.

[5] T. Uehara and R. Yanagimachi, "Microsurgical injection of spermatozoa into hamster eggs with subsequent transformation of sperm nuclei into male pronuclei," *Biology of Reproduction*, vol. 15, no. 4, pp. 467–470, 1976.

[6] Y. Zhao, H. Sun, X. Sha, L. Gu, Z. Zhan, and W. J. Li, "A review of automated microinjection of zebrafish embryos," *Micromachines*, vol. 10, no. 1, 2019.

[7] X. Gao, J. Yang, J. Wu, X. Xin, Z. Li, X. Yuan, X. Shen, and S. Dong, "Piezoelectric actuators and motors: materials, designs, and applications," *Advanced Materials Technologies*, vol. 5, no. 1, p. 1900716, 2020.

[8] G. Wang and Q. Xu, "Design and development of a piezo-driven microinjection system with force feedback," *Advanced Robotics*, vol. 31, no. 23-24, pp. 1349–1359, 2017.

[9] J. Liu, Z. Zhang, X. Wang, H. Liu, Q. Zhao, C. Zhou, M. Tan, H. Pu, S. Xie, and Y. Sun, "Automated robotic measurement of 3-d cell morphologies," *IEEE Robotics and Automation Letters*, vol. 2, no. 2, pp. 499–505, 2017.

[10] J. Ling, Z. Feng, D. Zheng, J. Yang, H. Yu, and X. Xiao, "Robust adaptive motion tracking of piezoelectric actuated stages using online neural-network-based sliding mode control," vol. 150, 2021, p. 107235.

[11] R. Ron-El, J. Liu, Z. Nagy, H. Joris, E. Van den Abbeel, and A. Van Steirteghem, "Intracytoplasmic sperm injection in the mouse*," *Human Reproduction*, vol. 10, no. 11, pp. 2831–2834, 1995.

[12] A. Ergenc, M.-W. Li, M. Toner, J. Biggers, K. Lloyd, and N. Olgac, "Rotationally oscillating drill (ros-drill) for mouse icsi without using mercury," *Molecular Reproduction and Development*, vol. 75, pp. 1744–1751, 2008.

[13] K. Ediz and N. Olgac, "Microdynamics of the piezo-driven pipettes in icsi," *IEEE Transactions on Biomedical Engineering*, vol. 51, no. 7, pp. 1262–1268, 2004.

[14] G. Wang and Q. Xu, "Design and precision position/force control of a piezo-driven microinjection system," *IEEE/ASME Transactions on Mechatronics*, vol. 22, no. 4, pp. 1744–1754, 2017.

[15] W. Johnson, C. Dai, J. Liu, X. Wang, D. K. Luu, Z. Zhang, C. Ru, C. Zhou, M. Tan, H. Pu, S. Xie, Y. Peng, J. Luo, and Y. Sun, "A flexure-guided piezo drill for penetrating the zona pellucida of mammalian oocytes," *IEEE Transactions on Biomedical Engineering*, vol. 65, no. 3, pp. 678–686, 2018.